

# Magnetohydrodynamic Simulation of the X2.2 Solar Flare on 2011 February 15: I. Comparison with the Observations

S. Inoue

*School of Space Research, Kyung Hee University, Yongin 446-701, Korea*

inosato@khu.ac.kr

K. Hayashi,

*W. W. Hansen Experimental Physics Laboratory, Stanford University  
Stanford, CA 94305 USA*

T. Magara

*School of Space Research, Kyung Hee University, Yongin 446-701, Korea*

G. S. Choe

*School of Space Research, Kyung Hee University, Yongin 446-701, Korea*

and

Y. D. Park

*Korea Astronomy and Space Science Institute, Daejeon 305-348, Korea*

## ABSTRACT

We performed a magnetohydrodynamic (MHD) simulation using a nonlinear force-free field (NLFFF) in solar active region 11158 to clarify the dynamics of an X2.2-class solar flare. We found that the NLFFF never shows the drastic dynamics seen in observations, *i.e.*, it is in stable state against the perturbations. On the other hand, the MHD simulation shows that when the strongly twisted lines are formed at close to the neutral line, which are produced via tether-cutting reconnection in the twisted lines of the NLFFF, consequently they erupt away from the solar surface via the complicated reconnection. This result supports the argument that the strongly twisted lines formed in NLFFF via tether-cutting

reconnection are responsible for breaking the force balance condition of the magnetic fields in the lower solar corona. In addition to this the dynamical evolution of these field lines reveals that at the initial stage the spatial pattern of the foot-points caused by the reconnection of the twisted lines appropriately maps the distribution of the observed two-ribbon flares. Interestingly, after the flare the reconnected field lines convert into the structure like the post flare loops, which is analogous to EUV image taken by SDO. Eventually, we found that the twisted lines exceed a critical height at which the flux tube becomes unstable to the torus instability. These results illustrate the reliability of our simulation and also provide an important relationship between flare-CME dynamics.

## 1. Introduction

Solar active region (AR) 11158 emerged in the eastern solar hemisphere on February 11, which consists of bipolar fields showing the complicated behaviors including the strongly sheared and twisted motions (Jiang et al. 2012). Eventually, it produced one X-class flare and several M-class flares on February 2011 (Sun et al. 2012; Tziotziou et al. 2013; Nindos et al. 2012; Inoue et al. 2013 and Aschwanden et al. 2014). Fortunately, solar physics satellites, the Solar Dynamics Observatory (*SDO*), and *Hinode* (Kosugi et al. 2007) provide rich data with unprecedented temporal and spatial resolutions obtained by multi-wavelength observations, enabling us to further understand the dynamics of these solar flares, *e.g.*, Schrijver et al. (2011), Kosovichev (2011), Asai et al. (2012), Liu et al. (2012), Jing et al. (2012), Inoue et al. (2013) and Toriumi et al. (2013).

In general the solar flares are widely considered as release phenomena of free magnetic energy accumulated in the solar corona (Shibata & Magara 2011), it's therefore important matter to understand the three-dimensional (3D) magnetic field to know where the free energy is accumulated in the AR. Unfortunately we cannot directly measure the coronal magnetic field even by the state-of-art ground or space observations which provide only 2D vector magnetic field on the photosphere. In this kind of situation, nonlinear force-free field (NLFFF) extrapolation from the vector field is a solid tool due to allow us to show 3D view of the magnetic field (see Wiegmann & Sakurai 2012 in details). The Helioseismic and Magnetic Imager (HMI; Scherrer et al. 2012; Schou et al. 2012; Hoeksema et al. 2014) on board a (*SDO*) and the Solar Optical Telescope (SOT; Tsuneta et al. 2008) on board *Hinode* provide the vector field data, which were already applied to extrapolate the 3D magnetic field under the NLFFF approximation by earlier studies ( Wiegmann et al. 2012; Jiang & Feng 2013; Inoue et al. 2013 and Aschwanden et al. 2014). In common of them, they show

that the strongly twisted and sheared field lines are found to reside at close to the polarity inversion line (PIL) before the flare, which are confirmed to relax after the flare.

Some earlier studies analyzed the NLFFF and suggested the dynamics of the M6.6 or X2.2-class flares due to compare the NLFFF with multi-wavelength observations or NLFFF configurations before and after the flares. Wang et al. 2012 suggested the possibility of tether-cutting reconnection (Moore et al. 2001) in X2.2-class solar flare through multi-wavelength analysis. Sun et al. (2012) also analyzed the NLFFF, showing the energy distribution of it in space and temporal evolution as well as suggesting an evidence of the tether-cutting reconnection on the variation of the field lines connectivity before and after the flare. Liu et al. 2012 analyzed the NLFFF just before and after the M6.6-class solar flare and found that the strong coronal current system underwent an apparent downward collapse and a small current-carrying loop was produced closer to the surface, suggesting that the tether-cutting reconnection is a suitable model. More recently, Liu et al. (2013) estimated the twist of a field line and investigated the connectivity of a field line, consequently the obtained results were consistent with the tether-cutting magnetic reconnection model.

Inoue et al. (2013) also estimated the magnetic twist of the NLFFF before the X2.2-class flare in AR 11158, reconstructed by MHD relaxation method (Inoue et al. 2014) and found that the strongly twisted lines having more than a half-turn twist but less than one-turn are related to this flare because their footpoints well correspond to the location where the two-ribbon flares in Ca II image taken by SOT/*Hinode* are enhanced. This result indicates that the NLFFF is found to be stable state against an ideal MHD instability, in other words, the tether-cutting reconnection would be needed to generate the more strongly twisted lines with more than one-turn twist, which might have a potential to produce the eruptive phenomena.

However, because these NLFFFs, which are constructed in the steady state, cannot reveal the dynamics in the solar flares, we cannot verify the occurrence of tether-cutting reconnection. In this study, we explore the MHD dynamics of the X2.2 solar flare on 2011 February 15, using MHD simulation involving the NLFFF. This simulation can tell us the dynamics of the magnetic field in close to the real situation, and then enable us to directly compare the results to observations. In this paper we show the results focusing on an overview of the 3D dynamics of the magnetic field and comparison of them with observations. The detailed dynamics, *e.g.*, it associated with the complicated reconnection process during flare will be shown in next paper. This paper is constructed as follows. Our observational data and numerical method are described in Section 2. Our results are presented in Sections 3 and discussed in Section 4. Our conclusion is summarized in Section 4.

## 2. Observations and Numerical Method

### 2.1. observations

To extrapolate the NLFFF, we use the vector magnetic field shown in left panel of Figure 1(a), observed at 00:00 UT on 2011 February 15, approximately 120 minutes before the X2.2-class flare detected by HMI/*SDO*. The vector magnetic field covers a  $216 \times 216$  ( $\text{Mm}^2$ ) region, divided by a  $600 \times 600$  grid which is provided by the description of CEA projected and remapped vector magnetic field <sup>1</sup>. It is obtained using the very fast inversion of the Stokes vector (VFISV) algorithm (Borrero et al. 2011) based on the Milne–Eddington approximation. A minimum energy method ( Metcalf 1994; Metcalf et al. 2006; Leka et al. 2009) was used to resolve  $180^\circ$  ambiguity in the azimuth angle of the magnetic field. We also use extreme ultraviolet (EUV) images observed with  $94\text{\AA}$  and  $171\text{\AA}$  taken by Atmospheric Imaging Assembly (AIA; Lemen et al. 2012) on board *SDO* and Ca II H  $3968\text{\AA}$  images during the flare taken by *Hinode*, in order to compare with the NLFFF and MHD simulation. Ca II images were obtained using the Broadband Filter Imager of the SOT on board *Hinode*. The field of view corresponds to  $111.58'' \times 111.58''$  with a resolution of  $1024 \times 1024$  at 01:50:18 UT on February 15.

### 2.2. Numerical Method of the Nonlinear Force-Free Extrapolation

We carry out the NLFFF and MHD simulation according to the following equations,

$$\rho = |\mathbf{B}| \quad (1)$$

or

$$\frac{\partial \rho}{\partial t} = -\nabla \cdot (\rho \mathbf{v}) + \xi \nabla^2 (\rho - \rho_0) \quad (2)$$

$$\frac{\partial \mathbf{v}}{\partial t} = -(\mathbf{v} \cdot \nabla) \mathbf{v} + \frac{1}{\rho} \mathbf{J} \times \mathbf{B} + \nu \nabla^2 \mathbf{v}. \quad (3)$$

$$\frac{\partial \mathbf{B}}{\partial t} = \nabla \times (\mathbf{v} \times \mathbf{B} - \eta_i \mathbf{J}) - \nabla \phi, \quad (4)$$

---

<sup>1</sup><http://jsoc.stanford.edu/jsocwiki/ReleaseNotes>

$$\mathbf{J} = \nabla \times \mathbf{B}. \quad (5)$$

$$\frac{\partial \phi}{\partial t} + c_h^2 \nabla \cdot \mathbf{B} = -\frac{c_h^2}{c_p^2} \phi, \quad (6)$$

where NLFFF calculation employs the equation (1) as the density evolution in order to ease the relaxation by equalizing the Alfvén speed in space as shown in Inoue et al. (2013).  $\rho$  is mass density,  $\rho_0$  is an initial value of density where this density evolution is following Aulanier et al. (2010),  $\mathbf{B}$  is the magnetic flux density,  $\mathbf{v}$  is the velocity,  $\mathbf{J}$  is the electric current density, and  $\phi$  is a scalar potential. The last equation (6) is used to reduce deviation from  $\nabla \cdot \mathbf{B} = 0$  and was introduced by Dedner et al. (2002).

The length, magnetic field, density, velocity, time, and electric current density are normalized by  $L^* = 216$  Mm,  $B^* = 2500$  G,  $\rho^* = |B_0|$ ,  $V_A^* \equiv B^*/(\mu_0 \rho^*)^{1/2}$ , where  $\mu_0$  is the magnetic permeability,  $\tau_A^* \equiv L^*/V_A^*$ , and  $J^* = B^*/\mu_0 L^*$ , respectively. The non-dimensional viscosity  $\nu$  is set as a constant ( $1.0 \times 10^{-3}$ ), and the coefficients  $c_h^2$ ,  $c_p^2$  in equation (6) also fix the constant values, 0.04 and 0.1, respectively. Subscript  $i$  of  $\eta$  corresponds to 'NLFFF' or 'MHD'. These equation sets, normalize values and parameters are mostly identical to the previous our studies Inoue et al. (2013) except the density evolution described in equation (2).

A formulation of  $\eta_{NLFFF}$  is given by

$$\eta_{NLFFF} = \eta_0 + \eta_1 \frac{|\mathbf{J} \times \mathbf{B}| |\mathbf{v}|^2}{|\mathbf{B}|^2}, \quad (7)$$

which is slightly different from Inoue et al. 2013, where  $\eta_0 = 1.0 \times 10^{-5}$  and  $\eta_1 = 1.0 \times 10^{-3}$ . The vector field shown in Figure 1(a) is preprocessed in accordance with Wiegelmann et al. (2006) and a potential field applied to an initial condition of the NLFFF calculation is extrapolated using Green function method (Sakurai 1982). The observed tangential components of the magnetic field reside in the region enclosed by a dashed square, as shown the left panel in Figure 1(a); the outside region is fixed by the potential field, because we focused on the dynamics of the magnetic field in an early phase near the central area and constructing a field close to an equilibrium state numerically. Note that, according to the mathematical formula, this state mixing of the force-free field and the potential field cannot keep an equilibrium. Nevertheless, we employed this method in this study in order to avoid an effect from inconsistent force-free alpha residing outside area where the weak magnetic fields are dominated.

### 2.3. Numerical Method of the MHD Simulation

Next, we set MHD equations under the zero  $\beta$  approximation (Mikic et al. 1989 or Amari et al. 1996) due to the low  $\beta$  (0.01  $\sim$  0.1) coronal plasma where the time evolution of density is according to the equation (1) being similar with Amari et al. (1996), *i.e.*; these equations are identical to the NLFFF extrapolation method in Inoue et al. (2014) or Inoue et al. (2013) except the velocity limit is not imposed and the resistivity formulation is different.

Initial condition on the density is given by  $\rho_0 = |\mathbf{B}|$  in all MHD (also NLFFF) calculations. In this case, the density is modeled by equation (1); therefore, we cannot compare it with observational data exactly or discuss the time scale of the dynamics of the magnetic field, as the Alfvén time scale depends on this model. However, this formula might be more reasonable than that in the constant density, *e.g.*  $\rho = 1.0$  because the real coronal density is stratified due to gravity, then Alfvén wave is propagation effectively in the upper corona where the magnetic field is driven there. In addition to these, Inoue & Kusano (2006) showed the dynamics of a flux tube using two types of density; one is modeled by  $\rho = 1.0$  at every time, *i.e.*, the density variation is not considered. Another is obtained from a continuous equation (2). Consequently, both dynamics of the magnetic field are nearly identical at the early eruptive phase. We will discuss later again in this paper. A resistivity formula is given as an anomalous resistivity as following,

$$\eta_{MHD} = \begin{cases} \eta_0 & J < j_c, \\ \eta_0 + \eta_2 \left(\frac{J-j_c}{j_c}\right)^2 & J > j_c, \end{cases} \quad (8)$$

where  $\eta_2 = 5.0 \times 10^{-4}$ , and  $j_c$  is the threshold current, set to 30 in this study.

In this simulation, a numerical box with dimensions of  $216 \times 216 \times 216$  (Mm<sup>3</sup>) is given by  $1 \times 1 \times 1$  as a non-dimensional value. The grid number is assigned as  $300 \times 300 \times 300$ , which is  $2 \times 2$  binning from the original data. Regarding to the boundary conditions of NLFFF (Run A) and MHD relaxation processes (Run C), physical values on all of the boundaries are fixed (fixed boundary condition), except for the Neumann-type boundary condition on which the convenient potential  $\phi$  is imposed. On the other hand, in MHD simulations (Run B, and Run D-F), tangential components of the magnetic field are released on all of the boundaries (Released boundary conditions). The numerical scheme is quite identical to that in Inoue et al. (2014) or Inoue et al. (2013). The kind of simulation (NLFFF or MHD), equation of the density evolution, initial conditions, and boundary conditions used in each Run are summarized in table 1.

### 3. Results

#### 3.1. Results of the Nonlinear Force-Free Extrapolation

##### 3.1.1. 3D Magnetic Structure of NLFFF

We first show the 3D magnetic structure of NLFFF and compare it with EUV images taken by AIA/*SDO*. We call this NLFFF calculation Run A and all of Runs in this study are summarized in table 1. The upper panels in Figure 1 (a) shows the vector field map obtained from HMI, and EUV images with 94 Å and 171 Å, respectively. The 3D field lines are plotted over each image shown in the middle panels in Figure 1(b). In the lower corona, we found that the strongly sheared field lines are formed above PIL located between the sunspots in the central area. On the other hand, although the large loops extending to upper corona can roughly capture the corona loops in AIA images, these reconstructed field lines seem to be deviating from them as altitude increases.

We perform further NLFFF reconstruction on the basis of whole vector field, not partial reconstruction such as in Figure 1(b), in order to further explore the reason of this problem. Figure 1(c) shows the NLFFF according the above manner, not showing the noticeable difference from that in Figure 1(b). Consequently, the potential field and NLFFF do not work effectively well on the reconstruction of the magnetic field in the upper corona. This is already suggested by Inoue et al. (2014) that it might be difficult to reconstruct these overlying field lines exactly because they cannot keep steady state due to that they are expanding to the further upper area pointed out by Magara (2011).

##### 3.1.2. Physical Properties of the NLFFF

Next, we show the physical properties of NLFFF, in particular, focusing on how much the reconstructed field is in a force-free state, its stability, and how much magnetic twist is accumulated in it. Figure 2(a) shows a distribution of the force-free alpha where the vertical and horizontal axes represent the values of the force-free  $\alpha$  estimated on opposite footpoints of each field line. Like Inoue et al. (2013), these force-free alpha are estimated at 720 km approximately *i.e.* 1 grid size in this case above the photosphere, and the field lines are traced from the region where  $B_z < -250$  G. This result seems to be slightly larger scatter than that in previous our result of Inoue et al. (2013)(see Figure 2(a)) even though many points are aligned close to the line of  $y=x$  plotted in green. This might be due to the fine force-free  $\alpha$  compared to previous one residing in the vector field reduced by  $8 \times 8$  binning process.

We perform an MHD simulations using reconstructed NLFFF as an initial condition to find a state in details of the NLFFF where the tangential components of the magnetic field are released on the bottom boundary, employing the constant resistivity. These calculation are named as Run B. Figure 2(b) shows a temporal evolution of the kinetic energy  $(\rho|\mathbf{v}|^2)/2$  for Run B. Its value increases initially because NLFFF cannot meet an equilibrium state exactly in addition to further deviate from the initial state due to the release of the tangential components of the magnetic field on the bottom surface, consequently the velocity is generated. On the other hand, after that, this profile being decrease as time goes on, which suggests that the reconstructed field is being back to the potential field even on the disturbances derived from the velocity. Two insets in Figure 2(b) represent the 3D view of the field lines at  $t=0$  and  $t=15$ , marked by the circles. We clearly see that the twisted field lines at  $t=15$  become looser than the initial state  $t=0$ , *i.e.*, the NLFFF is in stable state and never shows the drastic dynamics as seen in the observations.

We also investigate the magnetic twist that is here defined by

$$T_n = \frac{1}{4\pi} \int \alpha dl, \quad (9)$$

$\alpha$  and  $dl$  are force-free  $\alpha(= \mathbf{J} \cdot \mathbf{B}/|\mathbf{B}|^2)$  and a line element of a field line, respectively. Figure 2(c) shows the 3D field lines over the  $B_z$  distribution. Orange lines represent the strongly twisted lines over the half-turn twist which are traced inside of the red contours ( $T_n = 0.5$ ) shown in Figure 2(d). Figure 2(e) represents the twist distribution on the positive polarity where these twists are plotted on the intense  $B_z$  more than 0.2 (=500G). This result indicates that the most of twists have a value less than one-turn, suggesting the stable against the kink mode instability. These results are quite same as previous our result in Inoue et al. (2013) even though some parts of NLFFF model are different.

### 3.2. Formation of the Strongly Twisted Lines in NLFFF

From above section showing the physical properties of NLFFF, we found that the NLFFF never shows a dramatic dynamics or eruption away from the solar surface, which is contrary to the observation (Schrijver et al. 2011). Therefore, there might be mechanism that excites the stable NLFFF into dynamic unstable phase to cause the observed eruptive phenomena. So we perform the MHD relaxation process using the NLFFF as an initial condition, which is similar manner with NLFFF calculation in Run A except a velocity limit is released and an anomalous resistivity described in equation (8) is set in this calculation, in order to form a further strongly twisted lines more than one-turn twist. Because the anomalous resistivity plays a role on enhancing the reconnection in the strong current re-

gion, we can expect it to generate the more strongly twisted lines through the reconnection than that formed in the NLFFF. Because the magnetic field is fixed at the bottom boundary during this calculation, more strongly twisted lines are formed without changing the original horizontal components on vector field, *i.e.*, map of the observed force-free  $\alpha$  on the vector field is not changed. We call this calculation Run C.

Figure 3 shows a temporal evolution of the kinetic energy for Run C. We clearly see the kinetic energy starts to accelerate after  $t=0.5$  and then increasing as time goes on. The result in Run C indicates that solution is deviating from the NLFFF, suggesting it converts into the dynamic phase through the reconnection due to the anomalous resistivity.

In order to confirm this suggestion we note in previous section, we see the 3D magnetic structure and estimate the twist of the magnetic field lines at  $t=1$  marked by the vertical dashed line in Figure 3, which just begins to convert into the dynamic phase. Figures 4(a) and (b) show the 3D view of the magnetic field at  $t=0$  *i.e.*, NLFFF and  $t=1$ . The twisted lines in orange at  $t=1$  look changed slightly from the initial NLFFF state even though the overlying field lines surrounding these twisted lines almost keep their original configurations during this period in Run C. We further see the distribution of the magnetic twist and 3D magnetic structure in Figures 4(c) and (d) to understand the more detailed magnetic structure at close to the PIL in the central area. Figure 4(c) shows that the most of twist values in NLFFF are less than one-turn as discussed in the above section, on the other hand, the strongly twisted lines with more than one-turn are generated at  $t=1$  as shown in Figure 4(d), indicating the locations of their footpoints marked by dashed circles in upper panel, and showing the field lines traced from there in the lower panel. Interestingly, the locations of these footpoints are close to those of sunquake detected by the helioseismology (Zharkov et al. 2011), being triggered at the footpoint of the erupting flux rope at early flare phase. In addition, the change of the field lines topology from  $t=0$  to  $t=1$  allows us to be reminiscent of the tether-cutting reconnection (Liu et al. 2012, Wang et al. 2012 and Liu et al. 2013).

Therefore, this results might suggest that the tether-cutting reconnection plays an important role on breaking the equilibrium state before the flare.

### 3.3. MHD Simulation of Eruptive Magnetic Fields

#### 3.3.1. 3D dynamics of Eruptive Magnetic Fields

We suggested in above section that the magnetic field with the strongly twisted line over one-turn can break the equilibrium condition and make the NLFFF convert into the dynamic phase. However its time evolution is not consistent in that simulation because

the three components of the magnetic field are fixed on the boundaries, which is clearly over condition meaning that the dynamics might be shown properly due to the inconsistent boundary condition. In this section, we therefore perform the MHD simulation using the magnetic field shown in Figure 4(b), which is braking the equilibrium state, as an initial condition where the tangential components are released on all the boundaries to discuss its time evolution. This calculation is called Run D.

We first show an overview of the 3D Dynamics of the magnetic field lines for Run D with vertical velocity ( $v_z$ ) in Figure 5. This result shows that the twisted field lines with more than half-turn twist, being formed at  $t=2$  in Figure 4(b), in orange erupt away from the solar surface even though the tangential components of the magnetic field are released on all the boundaries. Because of the release boundary condition, the tangential components are deviating from that of original vector field as time goes, which is relaxing toward them close to the potential field. The NLFFF obtained from Runs B and C-1 never show these dynamics with the constant resistivity, this result thus indicates that the strongly twisted lines over the one-turn twist formed in NLFFF are required in this active region to break the quasi-equilibrium state.

### 3.3.2. Comparison with Observational Data

We compare these simulation results with observational data obtained from to confirm a reliability of our simulation. Figure 6(a) shows the EUV images in  $171 \text{ \AA}$  taken by AIA/*SDO*. Figure 6(b) plots the contour of  $|B_z| = 0.25$  over the AIA images. EUV is strongly enhanced at PIL between the sunspot located in the central area, on the other hand, it is enhanced too at the location marked by red circle, being away from the central area. This location corresponds to edge of the negative polarity on the east side in Figure 6(b). From Figure 5, we can see that the part of one footpoints of the twisted field lines jump from the central area to the edge of the negative polarity too after  $t=2.5$  as suggested from Figure 6. Therefore, these observational results might support our simulation.

Next we compare our simulation results with Ca II image taken by *Hinode* satellite. We focus on investigating the reconnection of only the twisted lines with more than one third ( $T_n=0.3$ ) because Inoue et al. (2011), Inoue et al. (2012) and Inoue et al. (2013) suggested that these twisted line at close to the PIL are related to the two-ribbon flares where the Ca II image is strongly enhanced. In addition to this, in this study we analyze it at early eruptive phase as shown in Figure 7(a) because in the late phase the tangential components of the magnetic field on the bottom boundary are deviating gradually from observational one due to the released boundary condition.

Following Toriumi et al. (2013), the reconnected field lines are estimated using the spatial variance of the field lines connectivity, which is allowed only by the magnetic reconnection. The formulation is defined by the following equation;

$$\delta(\mathbf{x}_0, t_n) = |\mathbf{x}_1(\mathbf{x}_0, t_{n+1}) - \mathbf{x}_1(\mathbf{x}_0, t_n)| \quad (|T_n| \geq 0.3),$$

where  $\mathbf{x}_1(\mathbf{x}_0, t_n)$  is a location of one footpoint of each field line at time  $t_n$ , which is traced from another footpoint at  $\mathbf{x}_0$ . Eventually, we calculate

$$\Delta(\mathbf{x}_0, t) = \int_0^t \delta(\mathbf{x}_0, t_n) dt_n, \quad (10)$$

where the enhanced region in  $I(\mathbf{x}_0, t)$  indicates memories in which the reconnection took place dramatically in the twisted lines. The left panel in Figure 7(b) exhibits the Ca II image taken by *Hinode*/SOT at the early flare phase and the middle and right panels show the distribution of  $I(\mathbf{x}_0)$  at  $t=2.0$  and  $t=4.0$ . Interestingly, the distribution of  $I(\mathbf{x}_0)$  is similar to that of the observed two-ribbon flares seen in the left panel in Figure 7(b). This result clearly shows that the two-ribbon flare is enhanced due to the reconnection of twisted lines, which is consistent with classical flare models(see Shibata & Magara 2011).

Finally, we show the field lines structure after the flare. Figure 8(a) shows the field lines over the flare-ribbons obtained from MHD simulation from which all of field lines are traced. Our simulation shows the post flare loops on the flare ribbons as often seen in observed EUV or Ca II images. We compare the simulation results with the EUV image with 94 Å taken by AIA/*SDO* shown in Figure 8(b). Before showing the comparison with the result of MHD simulation, Figure 8(c) shows the NLFFF after the flare, which is reconstructed from vector field at 03:00 UT on February 15, plotted over the EUV image. The NLFFF almost capture the post flare loops in EUV image shown in Figure 8(b). On the other hand, the field lines structure at  $t=10$  obtained from MHD simulation slightly deviates from the observed image and looks relaxation compared to those of NLFFF. Because the tangential components of the magnetic field are released on the bottom boundary, and then being toward close to the potential field. Nevertheless, they roughly capture the EUV image and this result would also support the reliability of our simulation.

## 4. Discussion

### 4.1. Formation of the CME

Above section, the MHD simulation showed the twisted lines initially embedded in the lower corona successfully erupt from the solar surface. However, its still unclear that these

twisted lines grow up to the CME or not. In order to clarify them, we discuss about the decay index profile being related to the torus instability (Kliem & Török 2006), which is an important factor in determining whether the flux tube can escape from the lower corona or not. The decay index refers to an estimation of a criterion for the torus instability and is given by the following equation:

$$n(z) = -\frac{z}{|\mathbf{B}|} \frac{\partial |\mathbf{B}|}{\partial z}, \quad (11)$$

where the threshold is at approximately  $n_c=1.5$  (Török & Kliem 2007). Because it is difficult to separate an external field from NLFFF, following Fan & Gibson (2007) or Aulanier et al. (2010), the decay index on the potential field is plotted in Figure 9(a), marked by a cross in the inset, where the strong twisted lines of NLFFF are embedded. From this result, the threshold is located at approximately  $h = 0.2$  corresponding to 63.2(Mm). Figure 9(b) shows a time evolution of selected twisted field line with more than half-turn where at  $t=0.0$  the twisted line exists in the lower area corresponding to less than  $h = 0.2$  at the top of the box. This indicates that the twisted line is stable against the torus instability. On the other hand, as time goes on, these cross over the critical height as a result of the initial eruption. This result might give an important scenario related to the dynamics of the flare-CME.

We present more detailed temporal evolution of the same selected twisted line in Figure 9(c) projecting them at each time on 2D plane with red line tracing a temporal evolution of the loop top. The dashed line indicates the critical height of the torus instability. Figure 9(d) shows the time variation of the loop top *i.e.*, the ascending velocity on appearance with the vertical dashed line where the twisted line is passing the critical height. This result does not exhibit sudden acceleration of the twisted line in this study, as shown in Aulanier et al. (2010) and Fan (2010), even though the loop top of the twisted line exceeds the critical height and its velocity looks to being increase slowly after  $t=5.0$ .

We might point out two causes to bring this problem. One is that the whole box is not large enough to trace the twisted lines for a long time. In addition, we set the rigid wall at all the boundaries, which is not able to expel the overlying field lines to the outside of the numerical domain, consequently the magnetic pressure is accumulated close to the boundary due to the twisted lines keep pushing the overlying field lines. Another is due to the bottom boundary condition *i.e.*, due to the release of the tangential components. Torus instability is driven by the poloidal field of the flux tube generated by the toroidal current carrying in it. However, the release condition for the tangential components relax the twisted lines, which means that hoop force driving the twisted lines upward is loosing gradually. These two factors preventing the twisted lines from the acceleration might work effectively on the dynamics of them. In other word, these twisted lines might have a potential for the solar

eruption if settling these problems on the size of numerical box and the boundary condition. Therefore, as prospective work, it is important matter how to fit the three component of the magnetic field obtained from the vector field data consistently into an induction equation, *i.e.*, would be required a data-driven simulation as presented in Cheung & DeRosa (2012).

#### 4.2. Depending on the Density Profile

We check the dynamics of depending on the density formula by replacing the equation (1) by the equation (2) where  $\xi$  is given by  $1.0 \times 10^{-4}$ . This calculation is called Run E. Figure 10(a) shows a temporal evolution of the kinetic energy for Run D and Run E, respectively. Both of them are a lot of similar profiles except we can see a little bit deviation at the late phase. On the other hand, Figure 10(b) shows an temporal evolution of the iteration number, which shows that Run E requires much more calculation time than that in Run D. 3D field lines structure marked by each circle in Figure 10(a) are shown in Figures 10(c) and (d). As a consequence, we conclude that the dynamics is almost same between them but the cost performance of Run D is much better than Run E, as shown in Inoue & Kusano (2006). This conclusion is also agreement with previous works done by Amari et al. (1996) and series of their papers.

#### 4.3. Depending on the Resistivity Formula

We further perform an MHD calculation (Run F) replacing the anomalous resistivity by constant one to show a dynamics of depending on the resistivity formula too. Figure 11(a) shows a temporal evolution of the maximum value of current density ( $=|\mathbf{J}|_{max}$ ) measured above 3600(km) for Run D and Run F, respectively, which can exclude the strong current density existing close to the photosphere. Although the value of Run D initially undergoes sudden decrease and is keeping less than one in Run F during the calculation, this sudden decrease is probably due to the diffusive effect derived from the anomalous resistivity. On the other hand, because the critical current set in the anomalous resistivity corresponds to the value 30, it works around by  $t=3$ . Nevertheless, temporal evolutions of the kinetic energy for Run D and Run F shown in Figure 10(b) are quite similar profiles although we can see a little bit deviation between them. Furthermore 3D field lines structure and color map of  $|\mathbf{J}|$  for Run D and Run E shown in Figures 10(c) and (d) are almost same too even at  $t=5.0$ . Form these results, in this case the anomalous resistivity dose not work effectively well on the dynamics while the twisted lines are ascending. However, note that the reconnection is very important to form the strongly twisted lines in the lower corona to launch from the

solar surface, after that it would take place only accompanied with ascending of the twisted lines pointed out by Inoue & Kusano (2006).

## 5. Summary

We performed the MHD simulation combined with NLFFF and show an overview of the dynamics of the magnetic field at early eruptive phase of the X2.2-class flare, and compared with observational results. The NLFFF is in a stable state against the kink mode instability (also confirmed by Inoue et al. 2013) and even any other perturbations as long as reconnection dose not occur in the NLFFF. On the other hand, when the tether-cutting reconnection in NLFFF could form the strongly twisted lines with more than one-turn twist, then we found that it plays an important role on breaking the quasi-steady state in NLFFF. Consequently the NLFFF converts into the dynamic stage and the twisted lines can erupt away from the solar surface. This scenario is already suggested by the previous studies on analysis of NLFFF in AR 11158 by Wang et al. (2012) , Liu et al. (2012), Inoue et al. (2013) and Liu et al. (2013). As a result for comparing with the observations, distribution of the observed two-ribbon flares are explained well by map on the spatial variance of the footpoints due to the reconnection of the twisted lines. In addition to this, the post flare loops seen in the AIA image are captured by the field lines after the reconnection on the MHD simulation. Thus, these results could support the reliability of our simulation results.

However, the some detailed dynamics on the twisted lines have not yet been revealed. One is that how much dose the flux tube need the magnetic twist just before launching from the solar surface, in order to reach the threshold height of the torus instability. In this study, although only one case (Run D) was performed and then presented here, we have to investigate the dynamics of another twisted lines having the different twist values initially, which is extended from this study. Then we can expect to find the critical twist leading the torus instability. Another is to reveal the complicated magnetic reconnection while the twisted line is ascending. The detailed analysis extended from this paper will answer this question definitely.

On the other hand, our simulation left some problems. Although the twisted lines cross over the threshold height of the torus instability, we could not see the sudden acceleration shown in the previous theoretical studies done by *e.g.*, Török & Kliem (2007), Aulanier et al. (2010), and Fan (2010). In order to answer this problem, we should extend size of the numerical domain, modify or develop an advanced boundary condition fitting the three component of the magnetic field on the photospheric magnetic field consistently into the induction equation , such as a data-driven simulation would be required (Cheung & DeRosa

2012).

In addition, in this study the triggering reconnection to produce the twisted flux tube is induced by the anomalous resistivity. However, in general, photospheric motion or new emerging flux drives pre-existing strongly twisted lines into the dynamic phase (*e.g.*, van Ballegooijen & Martens 1989, Feynman & Martin 1995). Therefore, in the future, we must develop a simulation considering this observational information. Doing so will allow further physical insight into the onset and dynamics of flare-CME.

We are grateful to anonymous referees for helping us improve and polish this paper. S. I. was supported by the International Scholarship of Kyung Hee University. This work was supported by the Korea Astronomy and Space Science Institute under the R & D program (project No.2013-1-600-01) supervised by the Ministry of Science, ICT and Future Planning of the Republic of Korea. G. S. C. was supported by the National Research Foundation grant NRF-2010-0025403. The computational work was carried out within the computational joint research program at the Solar-Terrestrial Environment Laboratory, Nagoya University. Computer simulation was performed on the Fujitsu PRIMERGY CX250 system of the Information Technology Center, Nagoya University. Data analysis and visualization are performed using resource of the OneSpaceNet in the NICT Science Cloud. We are sincerely grateful to NASA/SDO and the HMI and AIA science team. Hinode is a Japanese mission developed and launched by ISAS/JAXA, with NAOJ as domestic partner and NASA and STFC (UK) as international partners. It is operated by these agencies in co-operation with ESA and NSC (Norway).

## REFERENCES

- Achwanden, M., Sun, X., Liu, Y. 2014, arXiv
- Amari, T., Luciani, J. F., Aly, J. J., & Tagger, M. 1996, ApJ, 466, L39
- Asai, A., Ishii, T. T., Isobe, H., et al. 2012, ApJ, 745, L18
- Aulanier, G., Démoulin, P., & Grappin, R. 2005, A&A, 430, 1067
- Aulanier, G., Török, T., Démoulin, P., & DeLuca, E. E. 2010, ApJ, 708, 314
- Borrero, J. M., Tomczyk, S., Kubo, M., et al. 2011, Sol. Phys., 273, 267
- Cheung, M. C. M., & DeRosa, M. L. 2012, ApJ, 757, 147

- Dedner, A., Kemm, F., Kröner, D., et al. 2002, *Journal of Computational Physics*, 175, 645
- Fan, Y., & Gibson, S. E. 2007, *ApJ*, 668, 1232
- Fan, Y. 2010, *ApJ*, 719, 728
- Feynman, J., & Martin, S. F. 1995, *J. Geophys. Res.*, 100, 3355
- Hoeksema, J. T., Liu, Y., Hayashi, K., et al. 2014, *Sol. Phys.*, in press
- Inoue, S., & Kusano, K. 2006, *ApJ*, 645, 742
- Inoue, S., Kusano, K., Magara, T., Shiota, D., & Yamamoto, T. T. 2011, *ApJ*, 738, 161
- Inoue, S., Shiota, D., Yamamoto, T. T., et al. 2012, *ApJ*, 760, 17
- Inoue, S., Hayashi, K., Shiota, D., Magara, T., & Choe, G. S. 2013, *ApJ*, 770, 79
- Inoue, S., Magara, T., Pandey, V. S., et al. 2014, *ApJ*, 780, 101
- Jiang, Y., Zheng, R., Yang, J., et al. 2012, *ApJ*, 744, 50
- Jiang, C., & Feng, X. 2013, *ApJ*, 769, 144
- Jing, J., Park, S.-H., Liu, C., et al. 2012, *ApJ*, 752, L9
- Kliem, B., Török, T. 2006, *Physical Review Letters*, 96, 255002
- Kosovichev, A. G. 2011, *apjl*, 734, L15
- Kosugi, T., Matsuzaki, K., Sakao, T., et al. 2007, *Sol. Phys.*, 243, 3
- Leka, K. D., Barnes, G., Crouch, A. D., et al. 2009, *Sol. Phys.*, 260, 83
- Lemen, J. R., Title, A. M., Akin, D. J., et al. 2012, *Sol. Phys.*, 275, 17
- Liu, C., Deng, N., Liu, R., et al. 2012, *ApJ*, 745, L4
- Liu, C., Deng, N., Lee, J., et al. 2013, *ApJ*, 778, L36
- Magara, T. 2011, *ApJ*, 731, 122
- Metcalf, T. R. 1994, *Sol. Phys.*, 155, 235
- Metcalf, T. R., Leka, K. D., Barnes, G., et al. 2006, *Sol. Phys.*, 237, 267
- Mikic, Z., Schnack, D. D., & van Hoven, G. 1989, *ApJ*, 338, 1148

- Moore, R. L., Sterling, A. C., Hudson, H. S., & Lemen, J. R. 2001, *ApJ*, 552, 833
- Nindos, A., Patsourakos, S., & Wiegelmann, T. 2012, *ApJ*, 748, L6
- Sakurai, T. 1982, *Sol. Phys.*, 76, 301
- Scherrer, P. H., Schou, J., Bush, R. I., et al. 2012, *Sol. Phys.*, 275, 207
- Schou, J., Scherrer, P. H., Bush, R. I., et al. 2012, *Sol. Phys.*, 275, 229
- Schrijver, C. J., Aulanier, G., Title, A. M., Pariat, E., & Delannée, C. 2011, *ApJ*, 738, 167
- Shibata, K., & Magara, T. 2011, *Living Reviews in Solar Physics*, 8, 6
- Sun, X., Hoeksema, J. T., Liu, Y., et al. 2012, *ApJ*, 748, 77
- Toriumi, S., Iida, Y., Bamba, Y., et al. 2013, *ApJ*, 773, 128
- Török, T., & Kliem, B. 2007, *Astronomische Nachrichten*, 328, 743
- Tsuneta, S., Ichimoto, K., Katsukawa, Y., et al. 2008, *Sol. Phys.*, 249, 167
- Tziotziou, K., Georgoulis, M. K., & Liu, Y. 2013, *ApJ*, 772, 115
- van Ballegoijen, A. A., & Martens, P. C. H. 1989, *ApJ*, 343, 971
- Wang, S., Liu, C., Liu, R., et al. 2012, *ApJ*, 745, L17
- Wiegelmann, T., & Sakurai, T. 2012, *Living Reviews in Solar Physics*, 9, 5
- Wiegelmann, T., Thalmann, J. K., Inhester, B., et al. 2012, *Sol. Phys.*, 281, 37
- Wiegelmann, T., Inhester, B., & Sakurai, T. 2006, *Sol. Phys.*, 233, 215
- Zharkov, S., Green, L. M., Matthews, S. A., & Zharkova, V. V. 2011, *ApJ*, 741, L35

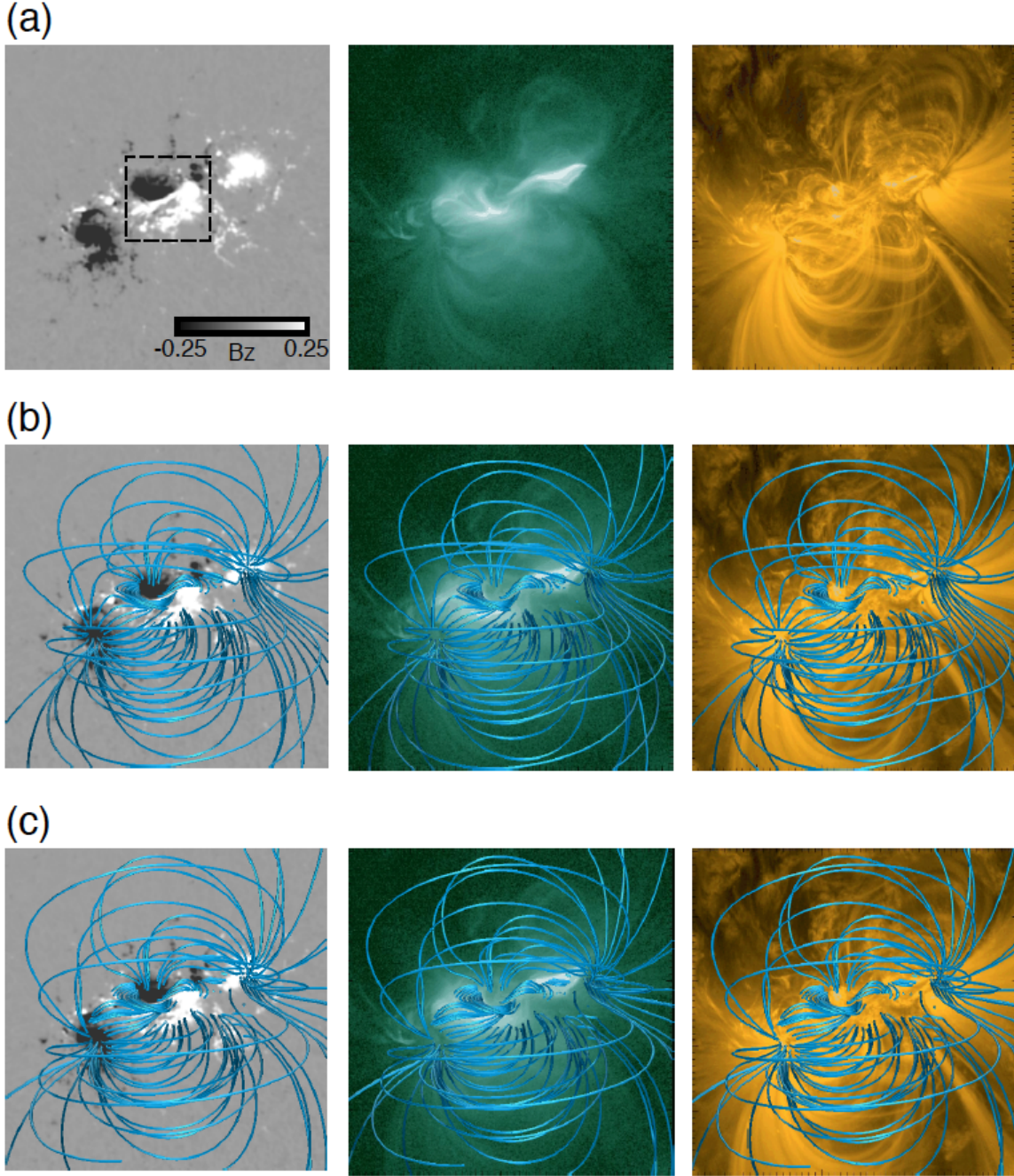


Fig. 1.— (a) Photospheric vector field (left), and EUV image with  $94 \text{ \AA}$  (middle), with  $171 \text{ \AA}$  (right) observed at 00:00 UT on 2011 February 15, taken by HMI and AIA on board *SDO*, are shown, respectively. These sizes are in the range of  $216 \times 216 \text{ (Mm}^2\text{)}$  and observed tangential components reside in the black dotted square ( $79.2 \leq x \leq 136.8$ ,  $86.4 \leq y \leq 144$ ) (Mm) during the calculation through this paper except (c), while other areas are fixed by the potential field. The value of  $B_z$  is normalized by  $2500 \text{ (G)}$ , non-dimensional value  $0.25$  corresponds to  $625 \text{ (G)}$ . (b) Field lines of the NLFFF are plotted over each image. (c) Field lines of the NLFFF which is reconstructed using whole vector field, not partial reconstruction such as (b), are plotted over each image.

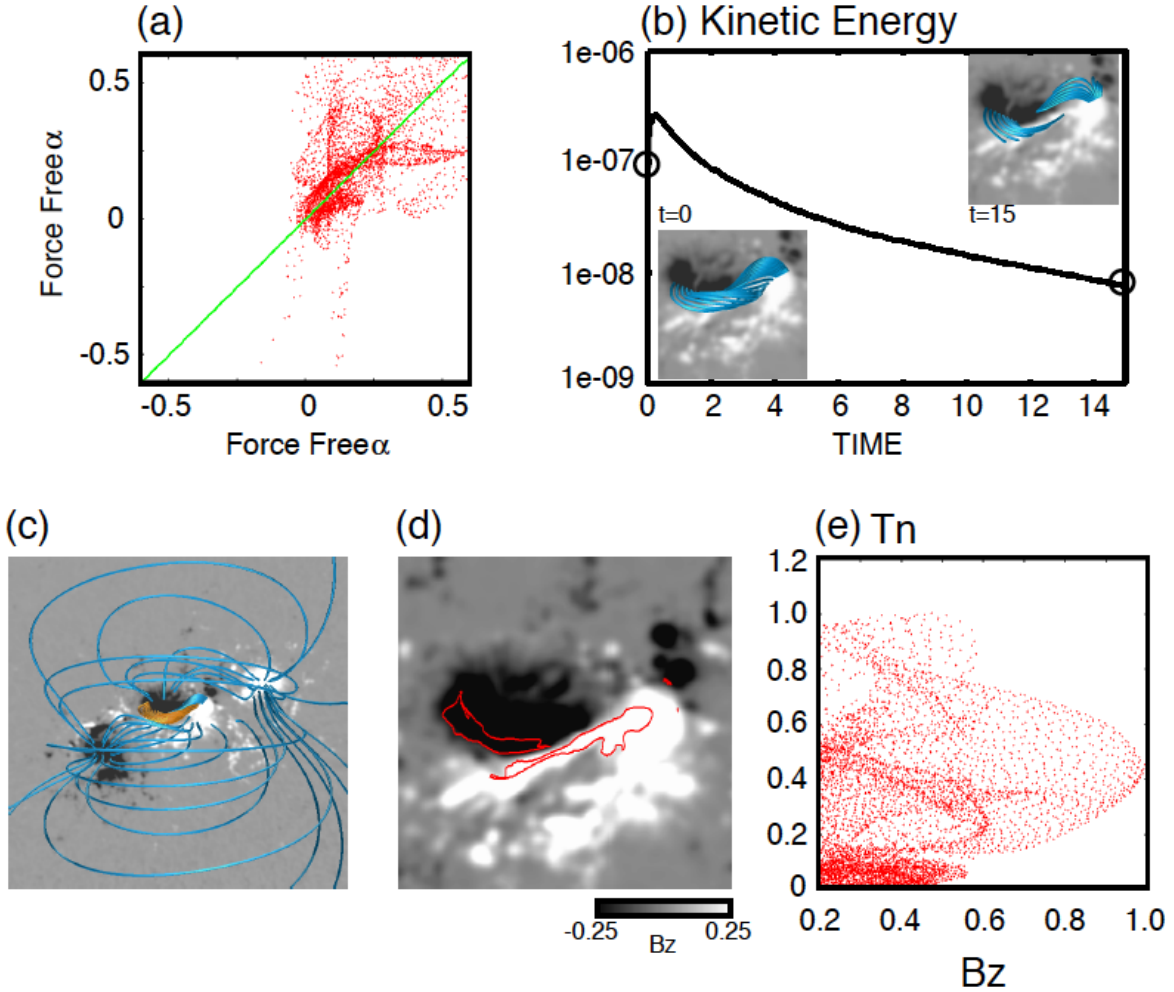


Fig. 2.— (a) Distribution of force-free  $\alpha$  map of the NLFFF. The closed field lines are focused and estimated in the central area within the dashed square in left panel of Figure 1(a). Vertical and horizontal axes represent the values of the force-free  $\alpha$  in opposite footpoints on each field line. These values are estimated in the plane at 720 km above the photosphere, and the field lines are traced from the region in which the values of the  $B_z$  are less than  $-0.1$  ( $=-250\text{G}$ ). Green line indicates the function of  $y = x$ . (b) Temporal evolution of kinetic energy in Run B. Two insets represent the 3D field lines at  $t=0$ , and  $t=15$ , respectively. Gray shows the  $B_z$  distribution. (c) 3D field lines in the NLFFF. Orange lines have the twist value more than half-turn ( $T_n > 0.5$ ) while the field lines with less than half-turn twist ( $T_n < 0.5$ ) are plotted in blue. (d) The red line indicates the contour of half-turn twist ( $T_n=0.5$ ). The inside of it is occupied by the strongly twisted lines ( $T_n > 0.5$ ). (e) Twist values are plotted on each positive  $B_z$  value more than  $0.2$  ( $=500\text{G}$ ).

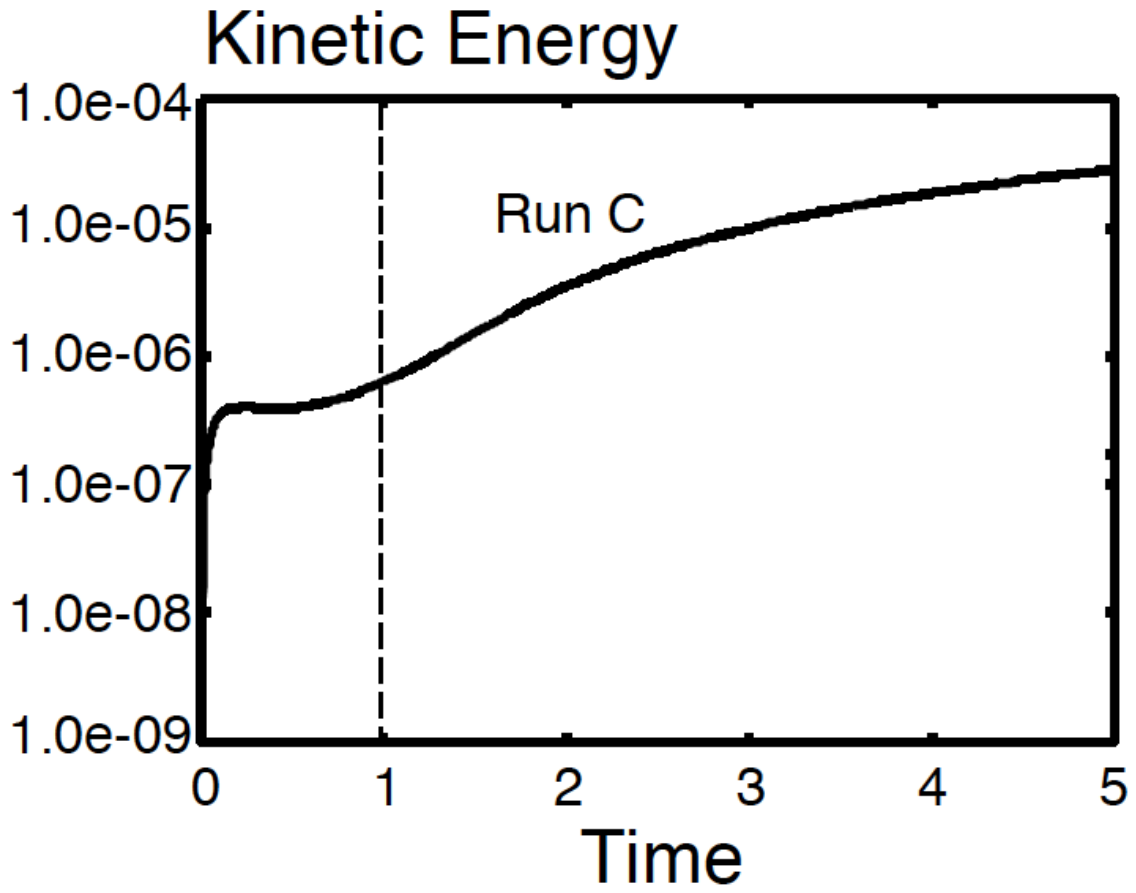


Fig. 3.— Temporal evolution of kinetic energy for Run C. The vertical dashed line indicates  $t=1$  at which the magnetic field is set up as an initial condition in Run D.

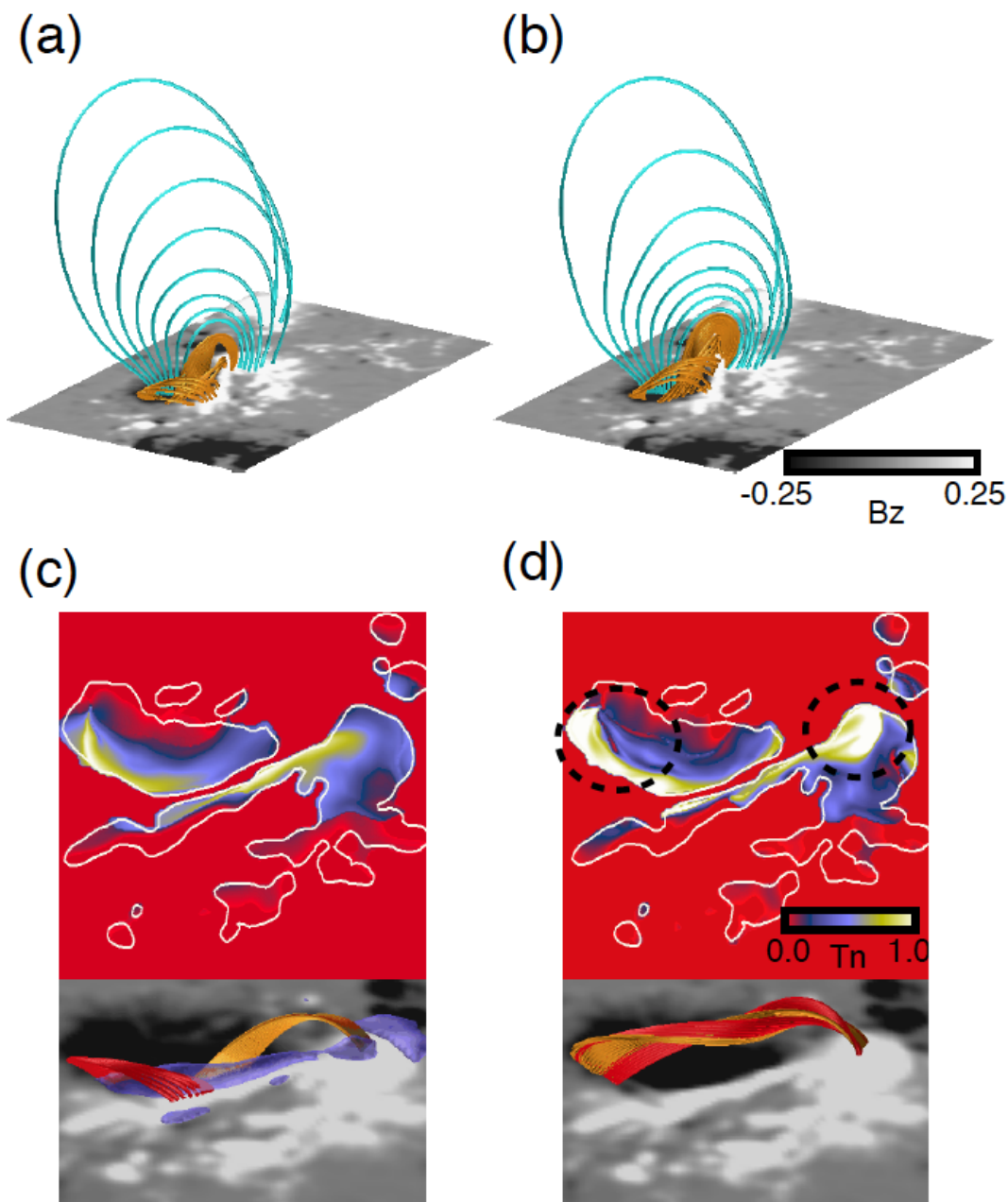


Fig. 4.— (a) and (b) show the 3D view of the field lines at  $t=0$  and  $t=1$ , respectively in Run C where these field lines are traced from same positions. The orange lines represent the strongly twisted lines with more than half-turn at  $t=1$  while blue lines represent overlying field lines surrounding the twisted lines. Upper panels in (c) and (d) show the twist distributions mapped on the bottom surface at  $t=0$  and  $t=1$ , respectively where the white line is a contour of  $|B_z|=0.25$ . The dashed circles indicate the location in which the twist value is more than one-turn. Lower panels show the field lines where red and orange field lines are traced from the regions surrounded by the each dashed circle. Purple surface represents the strong current  $|\mathbf{J}|=30$  corresponding to a critical current in the anomalous resistivity.

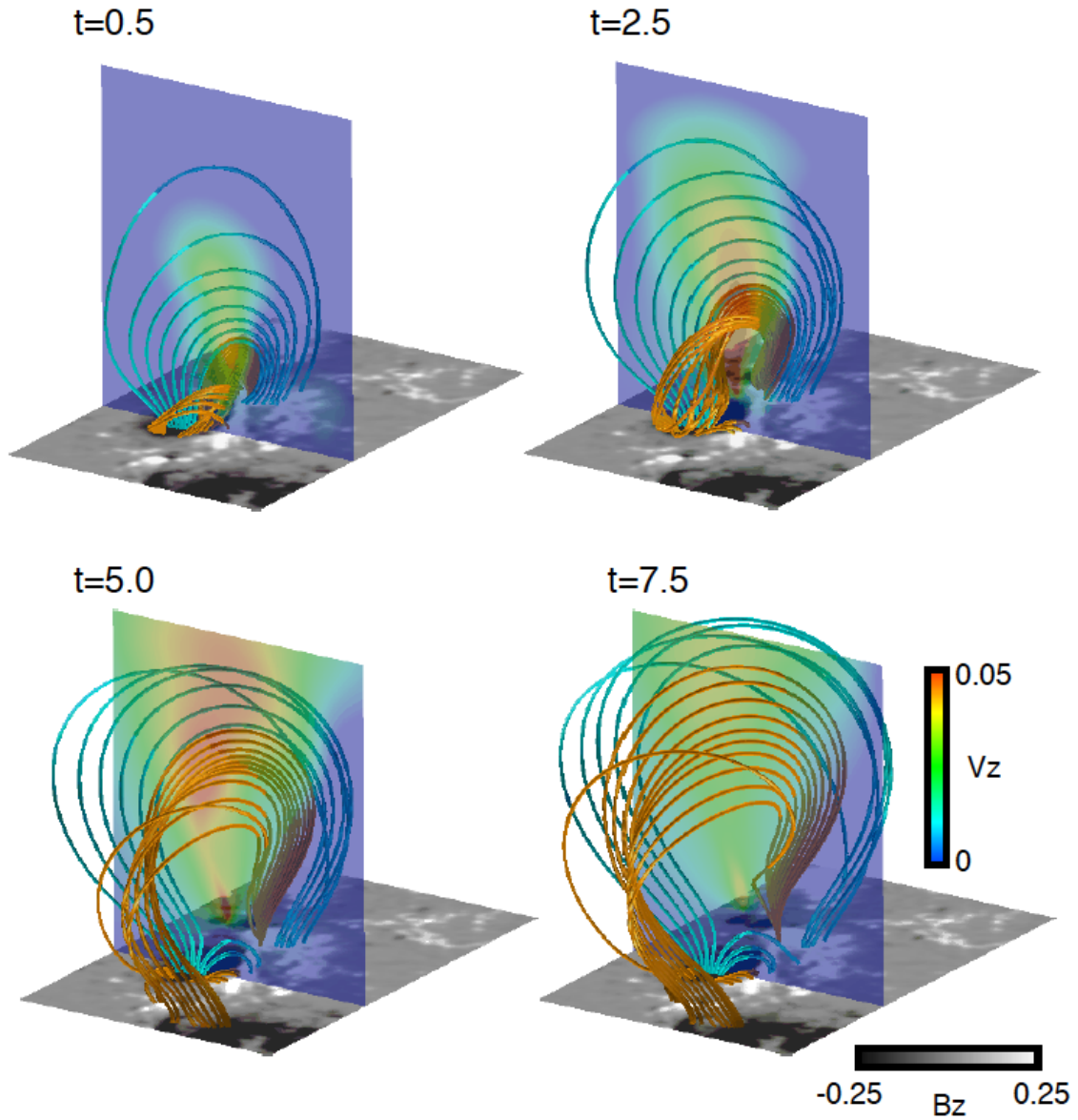


Fig. 5.— 3D dynamics of the magnetic field lines. Orange lines represent the twisted field lines with more than half-turn twist at  $t=0$  in Run D, *i.e.*,  $t=1$  in Run C while blue lines represent overlying field lines surrounding the twisted lines in orange.  $B_z$  distribution is drawn in gray and vertical velocity distribution is mapped in color.

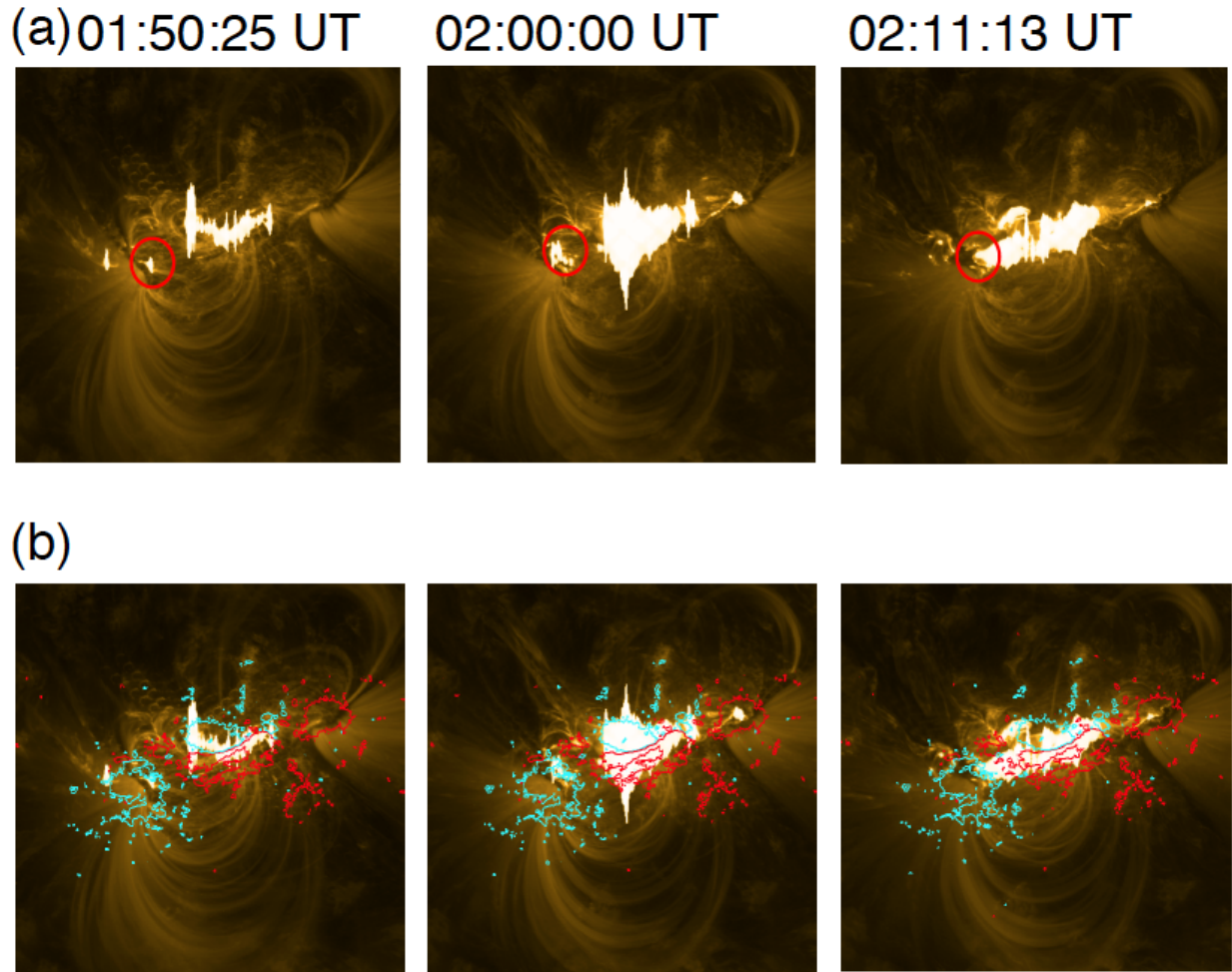


Fig. 6.— (a) EUV images with  $171 \text{ \AA}$  taken by AIA/*SDO* during the X2.2-class flare, observed at 01:50:25 UT, 02:00:00 UT, and 02:11:13 UT, respectively on February 15. (b) Red and blue lines are contours of  $|B_z|=0.25$ , plotted over (a).

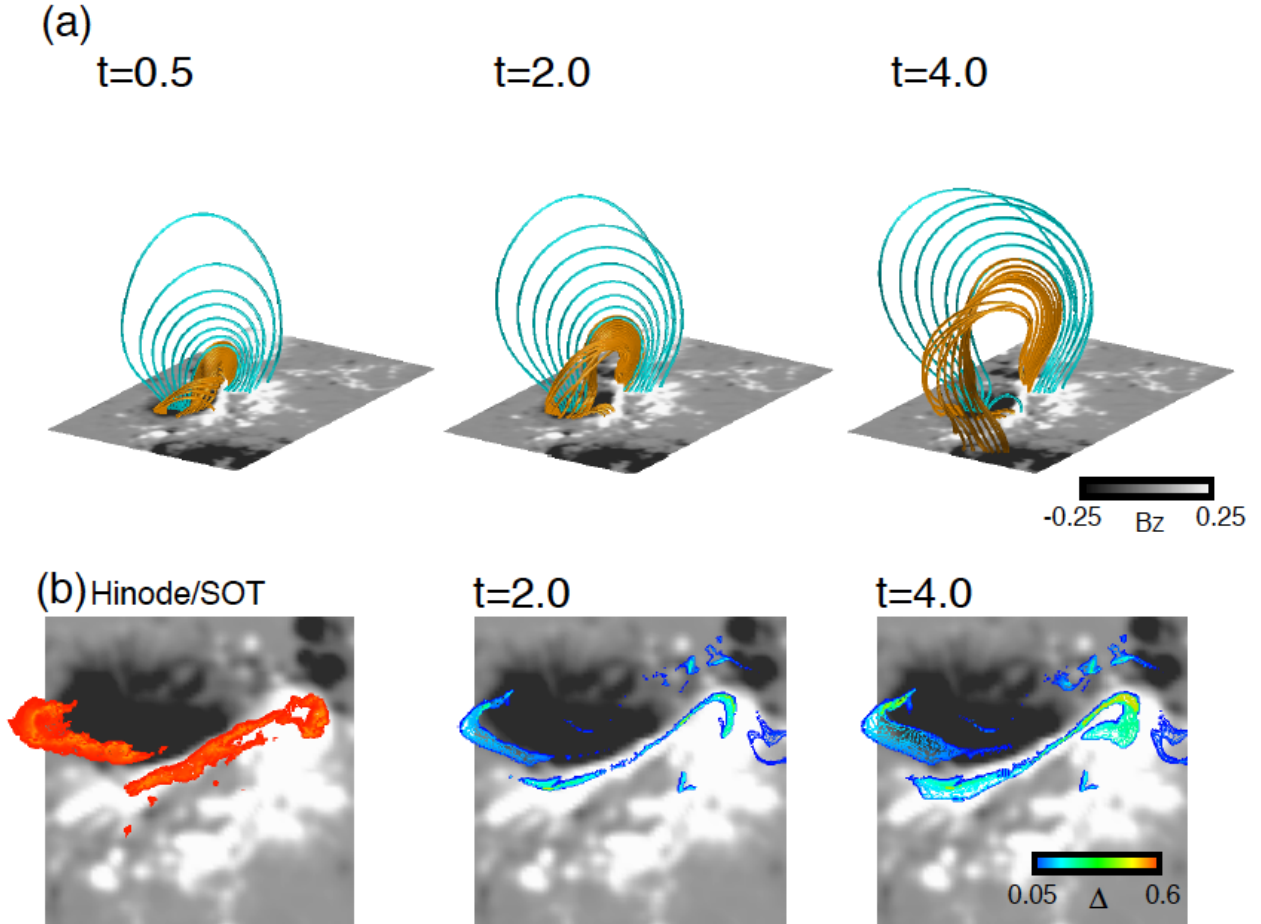


Fig. 7.— (a) Temporal evolution of the field lines from  $t=0.5$  to  $t=4.0$  in Run D, these are same format with Figure 5. The gray scale represents  $B_z$  distribution. (b) Left: Ca II image taken by FG/*Hinode* at 01:51 UT on February 15 is plotted over the  $B_z$  distribution. Middle and right:  $\Delta$  Maps of spatial variance of the footpoint caused by the reconnection of twisted line with more than one third ( $T_n=0.3$ ), which is defined in the equation (10), are plotted at  $t=2.0$  and  $t=4.0$  over the  $B_z$  distribution.

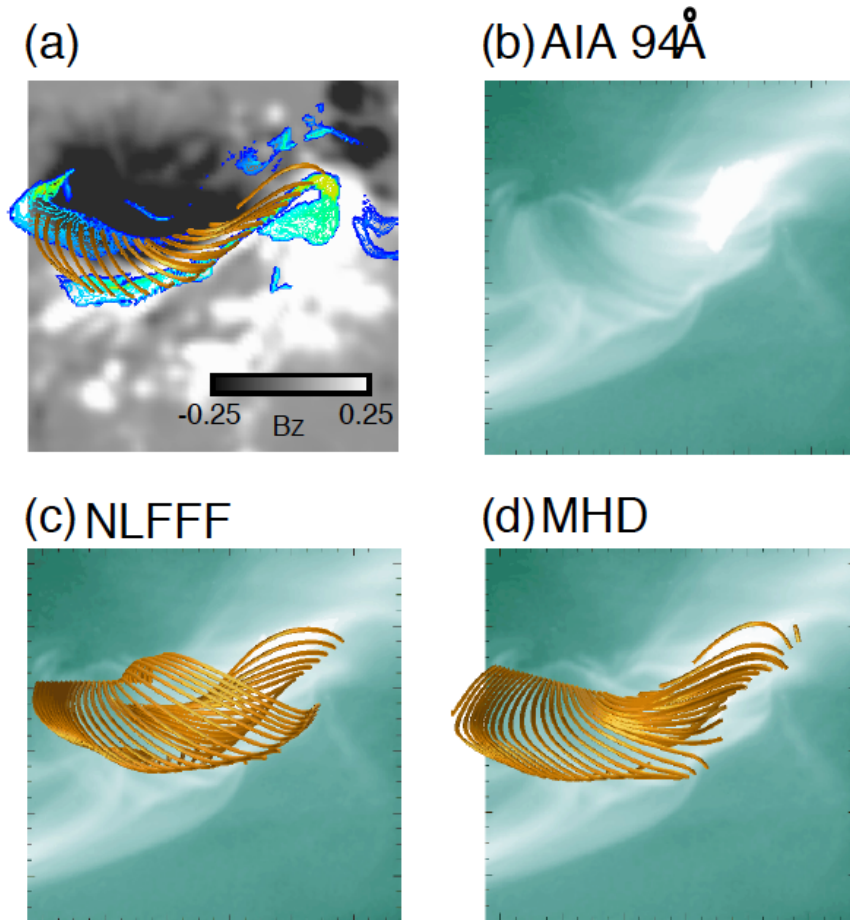


Fig. 8.— (a) Field lines are plotted with map on spatial variance of the footpoint caused by the reconnection at  $t=5.0$  being same format with Figure 7(b), over the  $B_z$  distribution in gray. (b) AIA image in  $94 \text{ \AA}$  taken by *SDO* observed at 02:29:50 UT on February 15. (c) Field lines of NLFFF, which are reconstructed from vector field observed at 03:00 UT on February 15, are plotted over the AIA image in (b). (d) Field lines from MHD simulation at  $t=10$  are plotted over the AIA image.

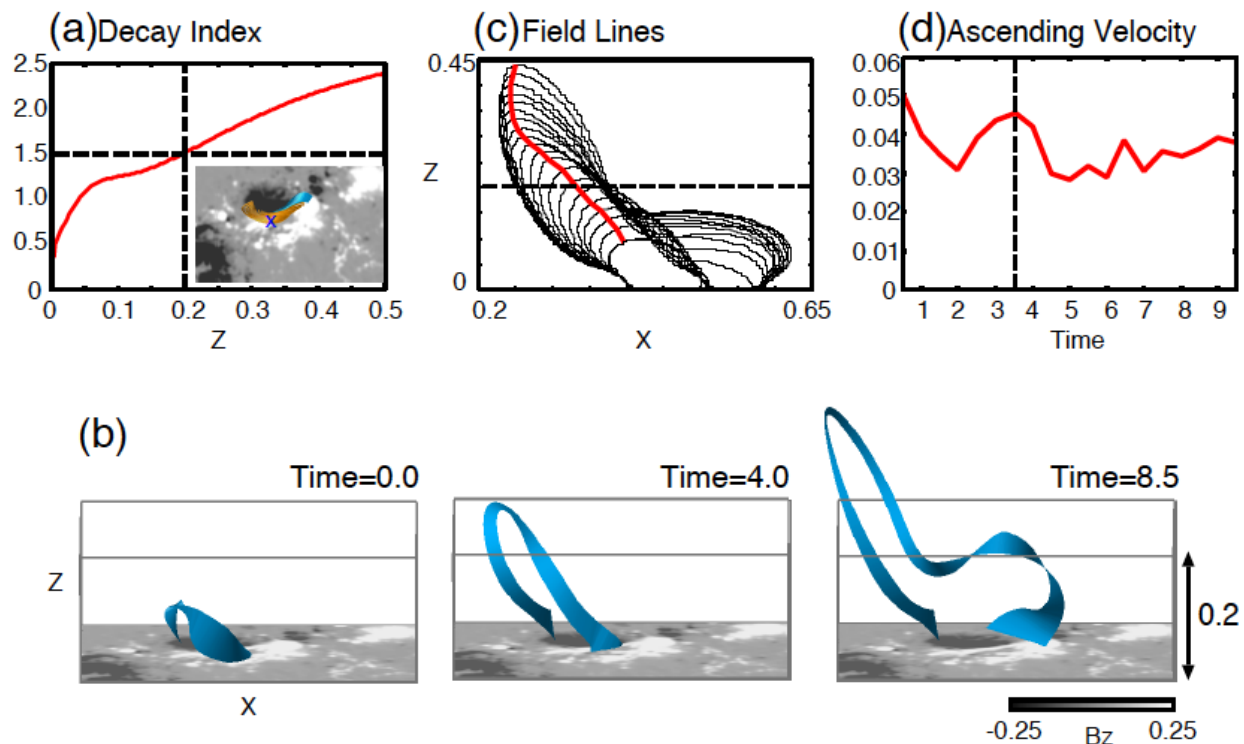


Fig. 9.— (a) Height profiles of the decay index on potential field are plotted, measured a cross in the inset in which the the NLFFF has strongly twisted lines (more than half-turn). The length is normalized by the 216(Mm), so  $h=0.2$  corresponds to 63.2(Mm). (b) A temporal evolution of selected twisted field lines are plotted in blue ribbon. The top of box corresponds to a critical height of the torus instability. (c) The same field lines in (b) are projected in  $x$ - $z$  plane from  $t=0.5$  to  $t=10$ . The red line traces the loop top and dashed line indicates the threshold height where twisted loop becomes torus instability. (d) The time variance of the loop top, *i.e.*, the ascending velocity of the twisted loop on appearance.

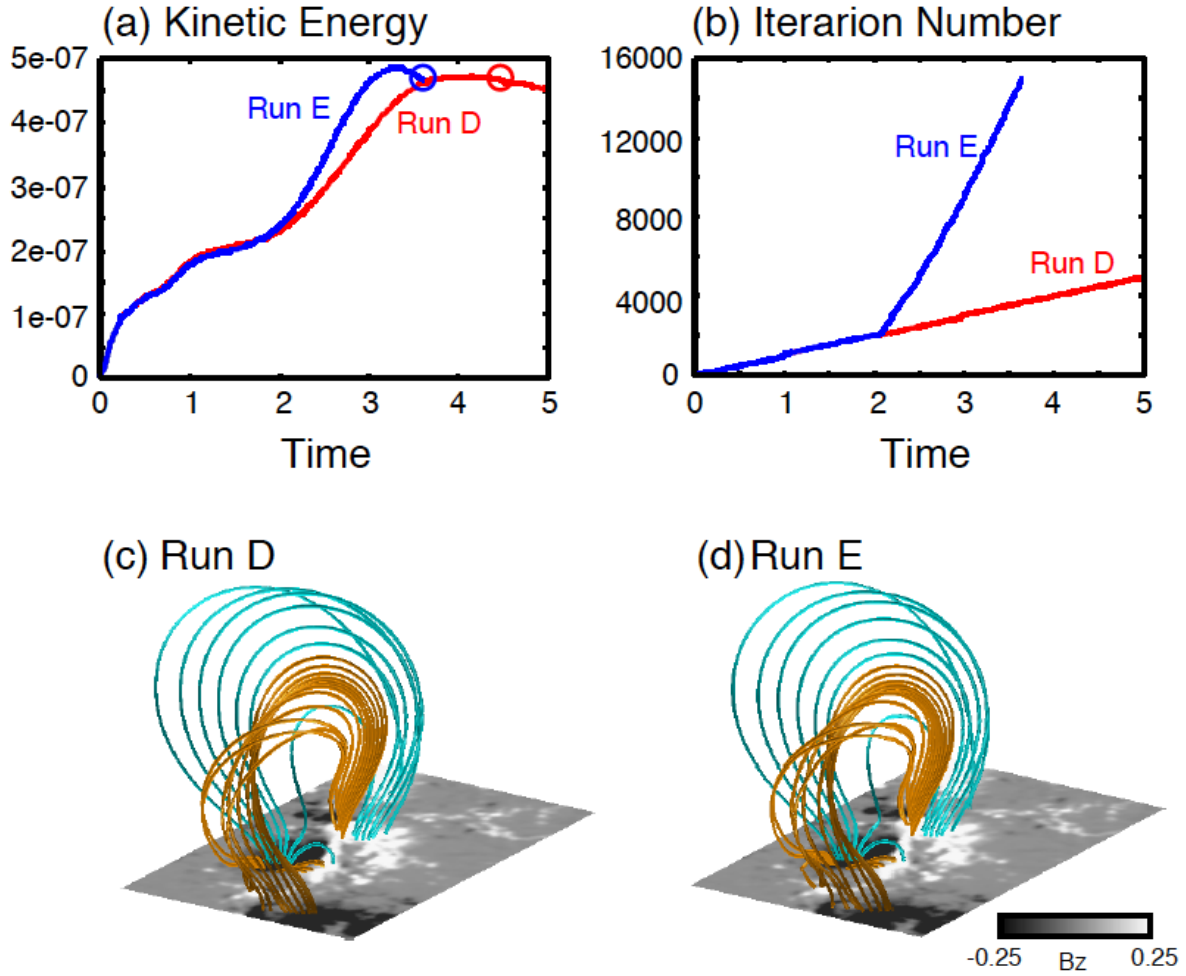


Fig. 10.— A temporal evolution of (a) kinetic energy and (b) iteration numbers for Run D and Run E in red and blue, respectively. 3D field lines structure in (c) Run D and (D) Run E are plotted. These formats are same as Figure 5.

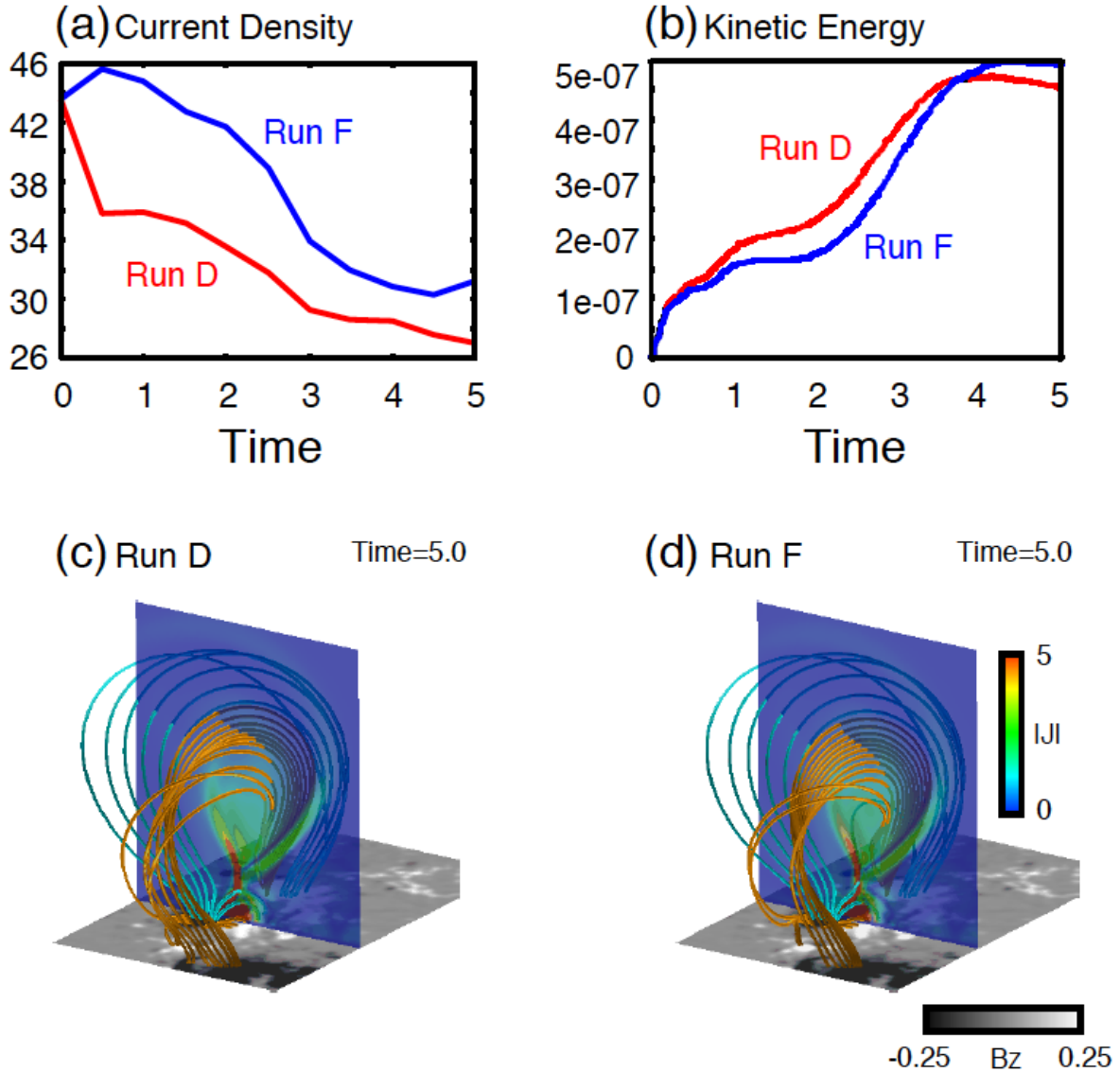


Fig. 11.— A temporal evolution of (a) maximum current density ( $|\mathbf{J}|_{max}$ ) measured above 3600 (km) corresponds to 5 grid above the photosphere and (b) kinetic energy for Run D and Run F in red and blue, respectively. The 3D field line structure with 2D  $|\mathbf{J}|$  map at  $t=5.0$  are plotted in (c) Run D and (d) Run F. Field lines format is same as Figure 5.

Table 1: Each Run for NLFFF or MHD simulation, employing equations of density evolution, resistivity formula, initial and boundary conditions.

Run	type	density	resistivity	Initial condition	Boundary condition
Run A	NLFFF	eq.(1)	eq.(7)	Potential field	Fix
Run B	MHD Simulation	eq.(1)	constant	NLFFF	Release
Run C	MHD Relaxation	eq.(1)	anomalous	NLFFF	Fix
Run D	MHD Simulation	eq.(1)	anomalous	$t = 1$ in Run C	Release
Run E	MHD Simulation	eq.(2)	anomalous	$t = 1$ in Run C	Release
Run F	MHD Simulation	eq.(1)	constant	$t = 1$ in Run C	Release